



Simulation and analysis of LPBF multi-layer single-track forming process under different particle size distributions

Liu Cao¹ · Wei Guan¹

Received: 24 September 2020 / Accepted: 22 March 2021 / Published online: 7 April 2021
© The Author(s), under exclusive licence to Springer-Verlag London Ltd., part of Springer Nature 2021

Abstract

Laser powder bed fusion (LPBF) has the advantages of rapid and customized production and has gradually been used in aerospace, biomedicine, and other fields. However, the current LPBF technology still faces many obstacles, such as the failure to fully explore the influence of the powder layer parameters (particle size distribution, thickness of spreading layer, etc.) on the LPBF multi-layer forming process. Based on the open-source discrete element method framework Yade and the open-source finite volume method framework OpenFOAM, the simulation flow for the LPBF multi-layer single-track process was established. Among them, the considered force influence factors included gasification recoil, surface tension, Marangoni effect, viscous force, mushy zone drag force, and gravity, and the considered thermal influence factors included gasification, convection, and radiation heat dissipation. In order to analyze the influence of particle size distribution and spreading layer thickness on the LPBF multi-layer process, the forming processes of the first eight layers of powder bed with three different particle size distributions and two different spreading layer thicknesses were calculated. Regarding the surface roughness of the formed layer, it was found that when the proportion of large-size particles increased, the surface roughness of the formed layer would increase. Regarding the actual thickness of the powder layer and the depth of the solidified track, it was found that they were mainly related to the thickness of the spreading layer, but were not affected by the particle size distribution. Regarding the porosity of the formed zone, it was found that when the spreading layer thickness was smaller, the higher the proportion of small-size particles, the lower the porosity of the formed zone; when the spreading layer thickness was larger, the smaller the proportion of large-size particles, the lower the porosity of the formed zone. This paper is expected to provide support for in-depth understanding of the effects of particle size distribution and spreading layer thickness on the LPBF multi-layer forming process.

Keywords Laser powder bed fusion · Particle size distribution · Spreading layer thickness · Surface roughness · Porosity · Numerical simulation

Abbreviations

α_1, α_2	Volume fractions of the metal-phase and the gas-phase in the element, respectively
t	Time
u	Velocity
$\bar{\rho}, \rho_1, \rho_2$	Mixed, metal-phase, and gas-phase densities, respectively
p	Pressure
τ	Stress tensor

$\bar{\mu}$	Mixed dynamic viscosity
\mathbf{I}	Unit matrix
\mathbf{g}	Gravitational acceleration
K_c	Drag coefficient of mushy zone ^[1]
f_{liquid}	Liquid-phase fraction
C_K	A custom small value, such as 10^{-6}
σ	Surface tension coefficient
κ	Interface curvature
n	Unit normal vector on the interface
T	Temperature
$\frac{d\sigma}{dT}$	Rate of change of σ with temperature
P_0	Standard atmospheric pressure
L_{gas}	Gasification latent heat of the metal
m	Molecular mass of the metal
k_B	Boltzmann constant
T_{gas}	Gasification temperature of the metal

✉ Liu Cao
caoliu@gzhu.edu.cn

¹ Institute for Systems Rheology, School of Mechanical and Electrical Engineering, Guangzhou University, Guangzhou 510006, Guangdong, China

\bar{c}_e, c_1, c_2	Equivalent ^[29] , metal-phase, and gas-phase specific heat capacities, respectively
\bar{k}	Mixed thermal conductivity
Q_{laser}	Laser energy density
h_{con}	Convective heat transfer coefficient on the interface
T_{con}	External convection temperature
σ_s	Stefan-Boltzmann constant
ε	Emissivity
T_{rad}	External radiation temperature
V_{metal}	Metal volume of the element
V_{sum}	Sum of the metal volume of the laser action elements under the same horizontal position
Δz	Element equivalent size, such as the side length of the cube
q_{laser}	Surface energy density of the laser
η	Laser absorption rate of the metal
P_{laser}	Laser power
R	Radius of the laser spot
x, y	Horizontal coordinates of the center point of the element
x_0, y_0	Horizontal coordinates of the center point of the laser spot
v_{laser}	Scanning speed of the laser

1 Introduction

As one of the main technologies of metal additive manufacturing, laser powder bed fusion (LPBF) uses a laser to melt metal powder layer by layer to form complex metal components [2, 3]. Thanks to its advantages of rapid and customized production, LPBF technology has gradually been applied in aerospace, biomedicine, and other fields [4, 5]. However, the current LPBF technology still faces many obstacles. For example, high dimensional accuracy and low porosity are still key indicators of concern to LPBF producers [6, 7].

At present, researchers have carried out a large number of experimental studies on LPBF process optimization. The research objects mainly include powder layer parameters (alloy type [8], particle size distribution [9], spreading layer thickness [10], etc.), laser parameters (laser power [11], spot size [12], etc.), scanning parameters (scanning speed [13], hatch space [14], scanning strategy [15], etc.). Sutton et al. [16] reviewed the commonly used powder characterization techniques, such as scanning electron microscopy, laser light diffraction, X-ray photoelectron spectroscopy, and differential thermal analysis. These powder characterization methods can be used to study particle morphology, chemistry, and microstructure, and then optimize the powder properties. Arsoy et al. [17] analyzed the influences of laser power, scanning

speed, hatch space, scanning strategy, and other process parameters on grain size and orientation for LPBF forming IN625 parts, and optimized the process parameters using methods such as response surface regression. The obtained experimental research results [8–17] provided good support for LPBF process optimization.

Similar to the high-power laser welding process [18], the LPBF forming process is also a typical high temperature and high transient physical process. At present, high-speed cameras [19, 20] and X-ray in-situ imaging technology [21, 22] can provide a means for people to observe the LPBF process in real time, but such methods are difficult to obtain three-dimensional and accurate real-time data, such as the changes in the three-dimensional shape of the molten pool. In view of this, numerical simulation technology has been more and more widely used in the field of LPBF [23–25]. The related numerical simulation technologies are mainly based on the mesoscopic scale, that is, first obtain the particle distribution of the powder bed [26, 27], and then calculate the heating effect of the laser on the metal particles to describe the dynamic behavior of the molten pool [28], and finally obtain the solidified track [29]. The current research objects of LPBF numerical simulation mainly include spreading layer thickness [30, 31], powder bed tightness [32], laser power [33], laser exposure time [34], scanning speed [35], and hatch space [36], in order to obtain a reasonable process parameter map. The author [37] calculated the LPBF spreading process based on discrete element method (DEM), analyzed the influence of different scraping methods and scraping speeds on the quality of the powder bed, and found that the powder bed tightness obtained by the scraping method of the roller (not rotating) was the highest. Le et al. [38] established a physics-based computational fluid dynamics (CFD) model to describe the fluid flow and heat transfer of the LPBF process. By calculating the molten pool flow patterns of the medium-deep and well-deep keyholes, the keyhole-induced porosity was predicted. The obtained simulation research results [23–38] provided some help for in-depth understanding of the LPBF forming process, but previous research [9] has shown that the LPBF process is expected to enter a quasi-steady state at least after the first six layers were formed. For example, the actual thickness of the powder layer is basically stable after the sixth layer was formed. The LPBF numerical simulation researches [23–25, 28–36, 38] that have been carried out are often limited to the first two layers of forming process, and the influences of powder layer parameters (particle size distribution, spreading layer thickness, etc.) on the LPBF multi-layer process were not fully analyzed. This is also the focus of this paper.

Based on the open-source DEM framework Yade and the open-source CFD framework OpenFOAM, this paper predicted the LPBF multi-layer single-track forming process at the mesoscopic scale. In order to analyze the influences of particle

size distribution and spreading layer thickness on the surface roughness of the formed layer, the actual thickness of the powder layer, the depth of the solidified track and the porosity of the formed zone, the forming processes of the first eight layers of powder bed with three different particle size distributions and two different spreading layer thicknesses were calculated, and the experimental results were compared and verified. This paper is expected to provide support for in-depth understanding of the effects of particle size distribution and spreading layer thickness on the LPBF multi-layer forming process.

2 Modeling approaches

2.1 Simulation of the spreading powder process

The premise of describing the LPBF forming process based on the mesoscopic scale is to obtain the particle distribution of the powder bed. In this paper, the open-source DEM framework Yade was used to simulate the spreading powder process [37]. Figure 1 shows the steps required to obtain the first layer of powder bed, including: (a) the diameters of the metal particles were measured with instruments such as a laser particle size analyzer, to obtain the particle size distribution of the metal powder; (b) regarding the morphology of metal particles as an ideal spherical shape, a “particle cloud” was generated above the substrate according to the particle size distribution curve, and the “particle cloud” is actually loose and suspended particles as one of the initial conditions for the powder spreading

simulation; (c) the “particle cloud” fell under gravity and laid loosely on the substrate; (d) the gap between the roller and the substrate was set to the required thickness of the powder bed, and the roller moved parallel to the substrate at a certain speed (during the spreading process, the normal and tangential contact between the particles and the force between the particles and the roller were considered); (e) after the roller had swept over the substrate, it stopped moving, and the radius and sphere center coordinates of the particles directly above the substrate were derived. Before Yade was used to calculate the spreading powder process, the set parameters mainly included material parameters (density, Young’s modulus, Poisson’s ratio, contact friction angle), particle size distribution, “particle cloud” position and roller moving speed, and other parameters adopted Yade’s default settings.

2.2 Mathematical model of the molten pool dynamics

After obtaining the particle distribution of the powder bed, the corresponding CFD model can be established to describe the dynamic behavior of the LPBF molten pool. In order to ensure the feasibility and efficiency of numerical calculations, this paper made the following two assumptions: the mass loss caused by metal gasification was not considered, and the flow behavior of liquid metal and gas was regarded as laminar flow of incompressible Newtonian fluid. The VOF model [39] was used here to track the distributions of metal-phase and gas-phase, the considered force influence factors included gasification recoil, surface tension, Marangoni effect, viscous force, mushy zone drag force [40], and gravity, and the considered

Fig. 1 Simulation of the spreading powder process: **a** particle size distribution; **b** generate a “particle cloud”; **c** particles laid loosely on the substrate; **d** spreading powder; **e** finish

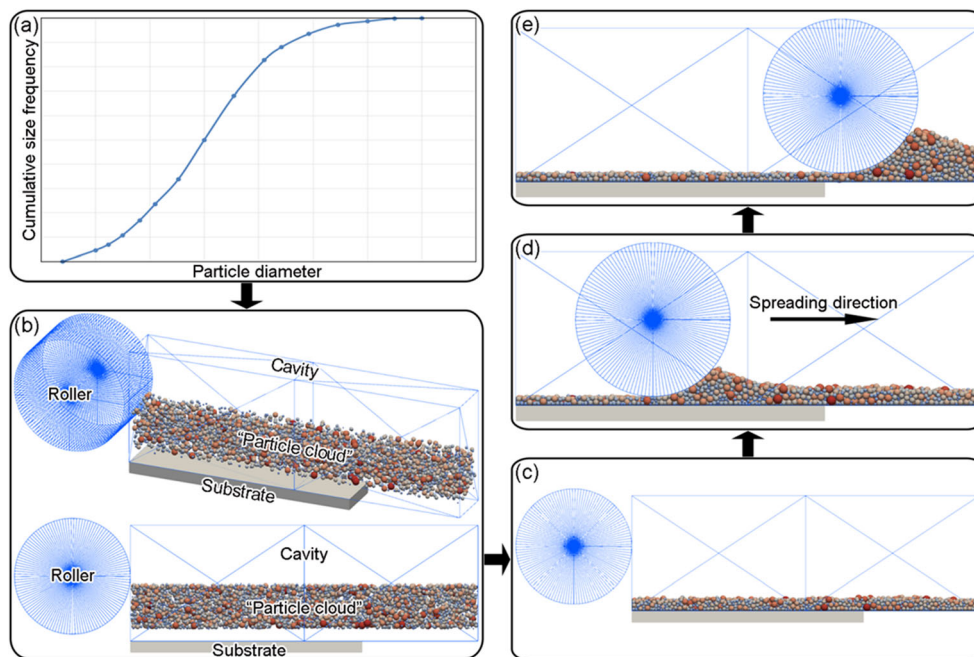
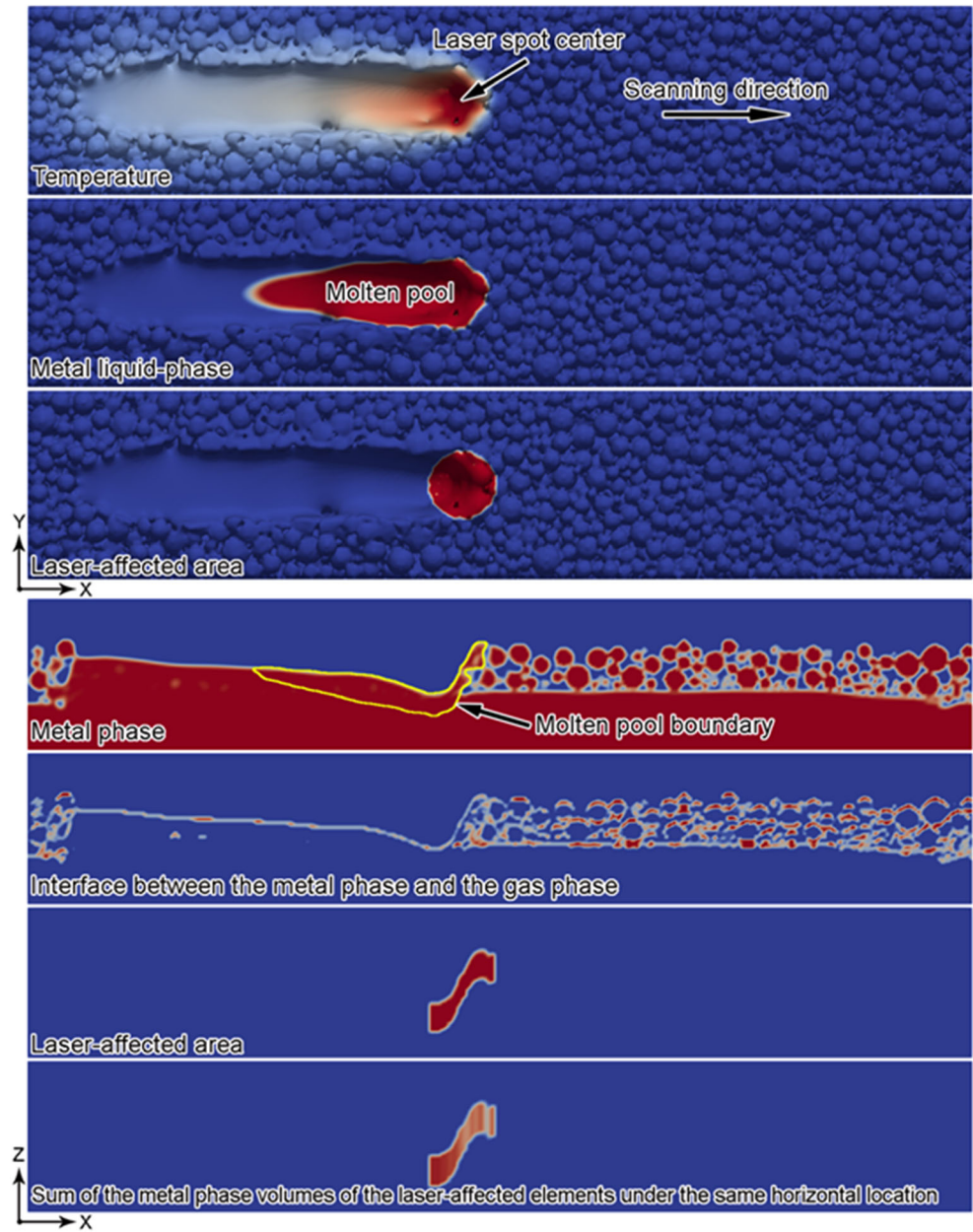


Fig. 2 Schematic diagram of the dynamic behavior of the molten pool and the laser heat source model (the red in the figure indicates the maximum value or positive meaning, and the blue indicates the minimum or negative meaning)



thermal influence factors included gasification, convection, and radiation heat dissipation. The dynamic model of the molten pool established was as follows:

$$\frac{\partial \alpha_1}{\partial t} + \nabla \cdot (\alpha_1 u) = 0 \tag{1}$$

$$\alpha_1 + \alpha_2 = 1 \tag{2}$$

$$\frac{\partial \bar{\rho} u}{\partial t} + \nabla \cdot (\bar{\rho} u \otimes u) = -\nabla \cdot p + \nabla \cdot \tau + \bar{\rho} g - \bar{\rho} K_C \left[\frac{(1-f_{liquid})^2}{f_{liquid}^3 + C_K} \right] u + \left\{ \sigma \kappa n + \frac{d\sigma}{dT} [(\nabla T - n(n \cdot \nabla T))] + 0.54 P_0 \exp \left[\frac{L_{gas} m}{k_B} \left(\frac{1}{T_{gas}} - \frac{1}{T} \right) \right] n \right\} |\nabla \alpha_1| \tag{3}$$

$$\frac{\partial \bar{\rho} c_e T}{\partial t} + \nabla \cdot (\bar{\rho} u c_e T) = \nabla \cdot (\bar{k} \nabla T) + Q_{laser} - |\nabla \alpha_1| \frac{2 \bar{\rho} c_e}{\rho_1 c_1 + \rho_2 c_2}$$

$$\left\{ h_{con}(T - T_{con}) + \sigma_s \varepsilon (T^4 - T_{rad}^4) + 0.82 \frac{L_{gas} m}{\sqrt{2\pi m k_B T}} P_0 \exp \left[\frac{L_{gas} m}{k_B} \left(\frac{1}{T_{gas}} - \frac{1}{T} \right) \right] \right\} \tag{4}$$

$$\nabla \cdot u = 0 \tag{5}$$

$$\bar{\rho} = \alpha_1 \rho_1 + \alpha_2 \rho_2 \tag{6}$$

$$\tau = 2\bar{\mu} \left[\left(\frac{1}{2} \nabla u + \frac{1}{2} (\nabla u)^T \right) - \frac{1}{3} (\nabla \cdot u) \mathbf{I} \right] \tag{7}$$

$$n = \frac{\nabla \alpha_1}{|\nabla \alpha_1|} \tag{8}$$

Fig. 3 Simulation flow for the LPBF multi-layer single-track process: (a1~a4) forming the first layer of powder bed (spreading powder→geometric model of the powder bed→CFD simulation→STL model of the solidified track surface); (b1~b4) forming the second layer of powder bed (spreading powder→geometric model of the powder bed→CFD simulation→STL model of the solidified track surface)

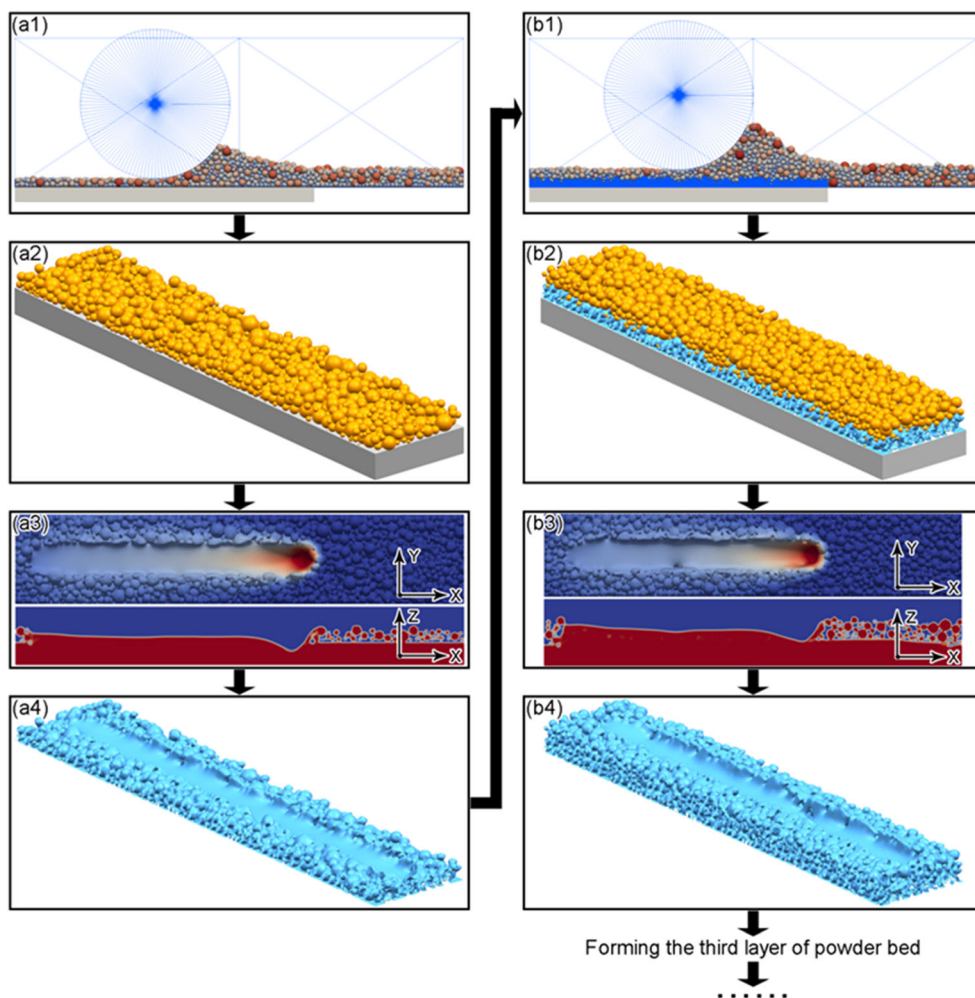


Table 1 Physical properties of 316L stainless steel

Parameter	Value	Unit
Density of metal	7270	kg/m ³
Specific heat of metal	790	J/(kg·K)
Thermal conductivity of metal	24.55	W/(m·K)
Solidus temperature	1658	K
Liquidus temperature	1723	K
Evaporation temperature	3090	K
Latent heat of melting	2.7 × 10 ⁵	J/kg
Latent heat of gasification	7.45 × 10 ⁶	J/kg
Viscosity of liquid metal	0.00345	Pa·s
Surface tension	1.6	N/m
Temperature of surface tension	− 8 × 10 ^{−4}	N/(m·K)
Molecular mass	9.3 × 10 ^{−26}	kg
Ambient pressure	101325	Pa
Boltzmann constant	1.380649 × 10 ^{−23}	J/K
Emissivity	0.26	
Stefan-Boltzmann constant	5.67 × 10 ^{−8}	W/(m ² ·K ⁴)
Density of air	1	kg/m ³
Specific heat of air	718	J/(kg·K)
Thermal conductivity of air	0.02346	W/(m·K)
Viscosity of air	1.48 × 10 ^{−5}	Pa·s

$$\kappa = -\nabla \cdot n \tag{9}$$

$$Q_{laser} = \frac{V_{metal}}{V_{sum}} \cdot \frac{q_{laser}}{\Delta z} \tag{10}$$

$$q_{laser} = \frac{2\eta P_{laser}}{\pi R^2} \exp\left(-2 \frac{(x-x_0-v_{laser}t)^2 + (y-y_0)^2}{R^2}\right) \tag{11}$$

The laser heat source model (Eqs. 10 and 11) is original. Fig. 2 is the schematic diagram of the dynamic behavior of the molten pool and the laser heat source model for the LPBF process. The metal particles melted after being heated by the laser to form a molten pool. The molten pool appeared dented under the combined influence of gasification recoil, surface tension, Marangoni effect, and other factors, and appeared in the shape of “droplet” on the horizontal surface. In order to effectively apply the laser energy to the powder bed, this paper first extracted the interface between the metal phase and the gas phase according to the distribution of α_1 ; then took (x_0, y_0) as the center and R as the radius to find the first layer elements

Table 2 Calculation schemes used to analyze the powder layer parameters

Calculation scheme	Spreading layer thickness (μm)	Particle size distribution	Layer number	Laser power (W)	Number of elements (ten thousand)	Number of threads used	Calculation time (hour)
a1	30	Type A	1	215	166.4	10	62.2
a2			2		204.8	10	112.7
a3			3		243.2	10	136.5
a4			4		246.4	10	149.9
a5			5		272	10	208.4
a6			6		294.4	10	206.0
a7			7		320	20	63.4
a8			8		342.4	20	164.9
b1	30	Type B	1	215	166.4	10	48.2
b2			2		204.8	10	68.7
b3			3		243.2	10	122.7
b4			4		246.4	10	135.7
b5			5		272	10	145.6
b6			6		294.4	10	189.2
b7			7		320	10	176.5
b8			8		342.4	20	168.5
c1	30	Type C	1	215	166.4	10	39.7
c2			2		204.8	10	37.1
c3			3		243.2	10	91.8
c4			4		246.4	10	45.8
c5			5		272	10	102.7
c6			6		294.4	10	119.1
c7			7		320	10	127.6
c8			8		342.4	10	164.8
d1	45	Type A	1	265	185.6	10	72.0
d2			2		243.2	10	139.3
d3			3		300.8	10	242.7
d4			4		294.4	10	277.4
d5			5		329.6	20	230.7
d6			6		371.2	30	187.2
d7			7		403.2	30	184.6
d8			8		438.4	40	136.3
e1	45	Type B	1	265	185.6	10	58.1
e2			2		243.2	10	127.4
e3			3		300.8	10	150.6
e4			4		294.4	10	236.5
e5			5		329.6	10	239.5
e6			6		371.2	20	220.1
e7			7		403.2	20	161.5
e8			8		438.4	30	110.1
f1	45	Type C	1	265	185.6	10	47.1
f2			2		243.2	10	65.5
f3			3		300.8	10	116.8
f4			4		294.4	10	126.1
f5			5		329.6	20	103.1
f6			6		371.2	20	113.4
f7			7		403.2	20	168.0
f8			8		438.4	20	149.3

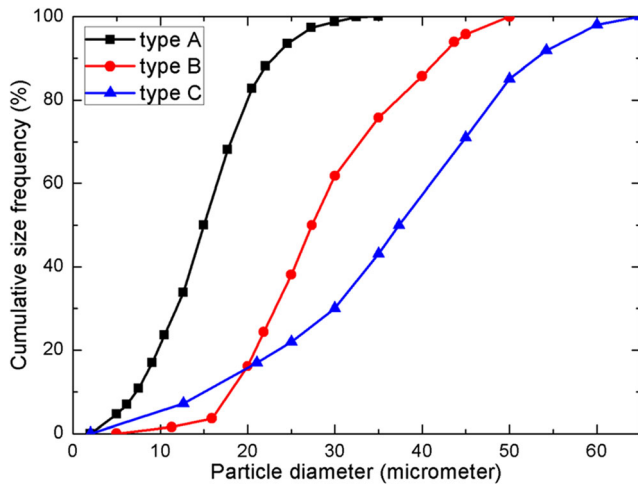


Fig. 4 Particle size distribution curves

under the laser action; then take the first layer elements as the starting point, found the elements within a certain distance along the direction of gravity, marked the found elements as the laser action elements; finally calculated the distribution of V_{sum} , and distributed the laser energy based on V_{metal} .

2.3 Simulation flow for the LPBF multi-layer single-track process

Figure 3 shows the simulation flow for the LPBF multi-layer single-track process. Its main steps include: (a) based on the

open-source DEM framework Yade, the spreading powder process was simulated, the radius and sphere center coordinates of the powder bed particles were derived, and the material parameters [40] set here were density (7270 kg/m^3), Young’s modulus (195 GPa), Poisson’s ratio (0.3), and contact friction angle (0.1); (b) according to the particle radius and sphere center coordinate data, the powder bed geometric model was generated with the aid of 3D modeling software, and pre-processing operations such as meshing were carried out; (c) based on the above theoretical model, the open-source finite volume method (FVM) framework OpenFOAM [40] was used to predict the dynamic behavior of the LPBF molten pool; (d) with the help of post-processing software, the solidified track surface data was extracted and the corresponding stereo lithography (STL) model was derived; (e) the obtained STL model was imported into Yade, and steps (a–d) were repeated to form the next layer of powder bed.

3 Results and discussion

3.1 Calculation parameters

The metal powder material used here was 316L stainless steel, and its alloy composition (mass percentage) was Fe 65.395%-Cr 17.0%-Ni 12.0%-Mo 2.5%-Mn 2.0%-Si 1.0%-P 0.045%-C 0.03%-S 0.03%. Table 1 shows the physical properties of 316L stainless steel calculated by JMatPro v7.0.

Fig. 5 Molten pool at the intermediate time and morphology of the final solidified track for each forming layer under calculation scheme a

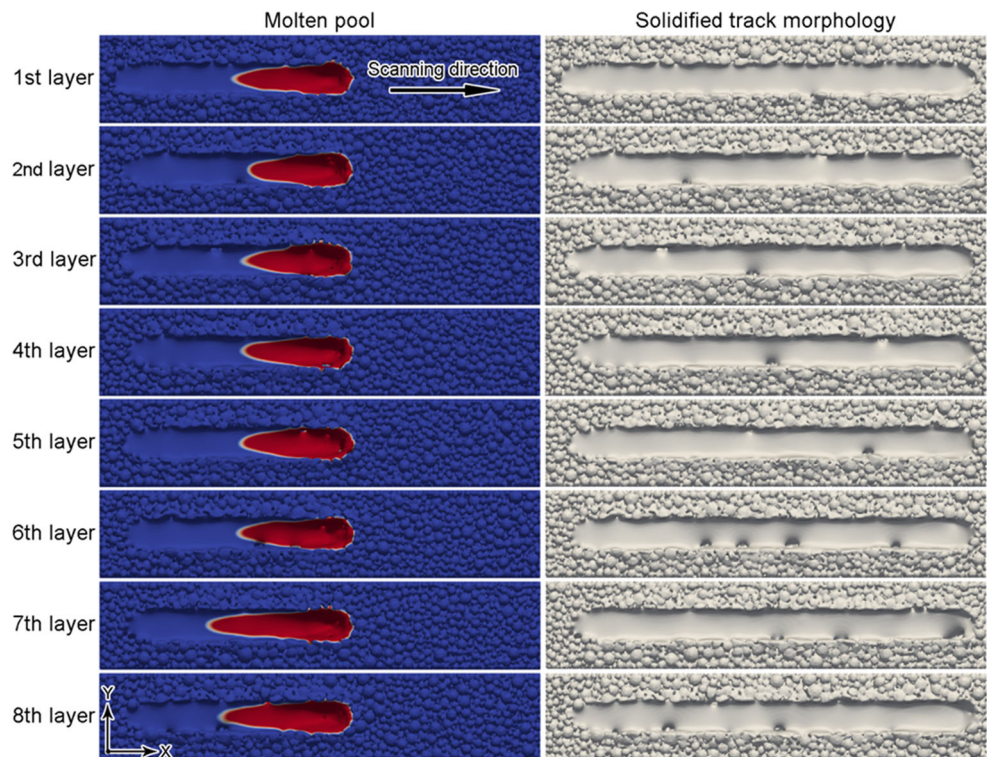
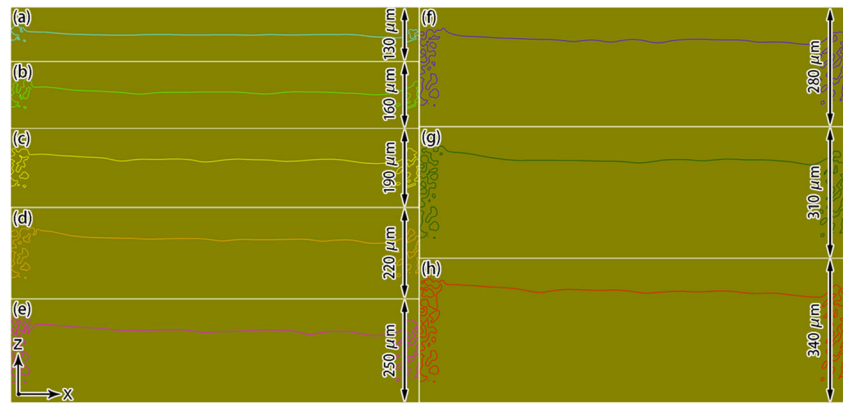


Fig. 6 Middle section of the solidified tracks for each forming layer under calculation scheme a



The focus of this paper is the influences of powder layer parameters (particle size distribution, spreading layer thickness) on the LPBF multi-layer forming process, such as the surface roughness of the formed layer, the actual thickness of the powder layer, the depth of the solidified track, and the porosity of the formed zone. To this end, the process schemes shown in Table 2 were calculated, with reference to the simulation flow shown in Fig. 3. Among them, the particle size distributions type A, type B, and type C referred to Ref. [9], and Fig. 4 shows the curves of the particle size distributions type A, type B, and type C. The mesh model sizes of all calculation schemes in Table 2 were *X*-direction (1000 μm), *Y*-direction (200 μm), and *Z*-direction (50 μm of the substrate + total thickness of the powder layers + 50 μm of the air layer). Taking the calculation scheme of forming the fourth layer of powder bed with the spreading layer thickness of 30 μm as an example, the mesh model size was *X*-direction (1000 μm), *Y*-direction (200 μm), and *Z*-direction (220 μm). In addition, the laser spot diameter was 70 μm , the scanning speed was 1 m/s, the laser absorption rate was 0.35, the ambient temperature was 300 K, the calculation time step was 2.5×10^{-7} s, and the computing resource configuration used was Intel Xeon Gold 6240 CPU (dual CPU, 72 threads, 128 GB memory).

Comparing the calculation time used for each calculation scheme in Table 2, it could be found that since the proportion of small-size particles of type A was significantly higher than that of types B and C, the calculation time required for type A was significantly longer. In addition, the calculation time was also affected by the spreading layer thickness, the current forming layer number, the number of threads used, and the number of schemes currently calculated by the workstation.

3.2 Influence of particle size distribution on the surface roughness of the formed layer

Figure 5 is the simulation result of forming each layer of powder bed under calculation scheme a. On the whole, the

forming process of each powder layer was basically similar, in which the metal particles were heated by the laser to form a molten pool, and the molten pool was basically kept in a droplet shape, then gradually solidified to form a pit, and finally, a solidified track was obtained. In order to analyze the influence of particle size distribution on the surface roughness of the formed layer, the *Y*-direction middle section of each layer of the solidified track was extracted here. It was believed that the height fluctuation degree of the top surface of the solidified track in the section could reflect the surface roughness of the solidified track. The height fluctuation degree of the top surface was obtained by calculating the arithmetic mean of the absolute value of the deviation from the average height at each point of the profile. Figure 6 shows the middle section of each layer of solidified track under calculation scheme a. In order to visually compare the middle section results of different layers of solidified track, Fig. 7 summarizes the middle section results of each layer of solidified track under calculation scheme a~f. It can be seen intuitively from Fig. 7 that for one of calculation schemes a~f, the height fluctuations of each layer of the solidified tracks were not much different, so it can be concluded that the surface roughness of each formed layer was basically the same under the same calculation scheme. When the spreading layer thickness was 30 μm (Fig. 7a~c), the solidified track height fluctuation was the smallest when the particle size distribution was type A, and the maximum when the particle size distribution was type C. The same conclusion can be drawn by comparing the results when the spreading layer thickness was 45 μm (Fig. 7d~f), so it can be concluded that the particle size distribution has a greater influence on the surface roughness of the formed layer. When the particle size distribution was type A, comparing the calculation results under different spreading layer thicknesses (Fig. 7a, d), it can be found that the solidified track height fluctuations under the two calculation schemes were not much different. This conclusion is also true when the particle size distributions were type B (Fig. 7b, e) and type C (Fig. 7c, f), so it can be concluded that the spreading layer

Fig. 7 Summary of the middle section of the solidified tracks for each forming layer under each calculation scheme (different colors represent the middle section of different layers of solidified tracks): **a** calculation scheme a; **b** calculation scheme b; **c** calculation scheme c; **d** calculation scheme d; **e** calculation scheme e; **f** calculation scheme f

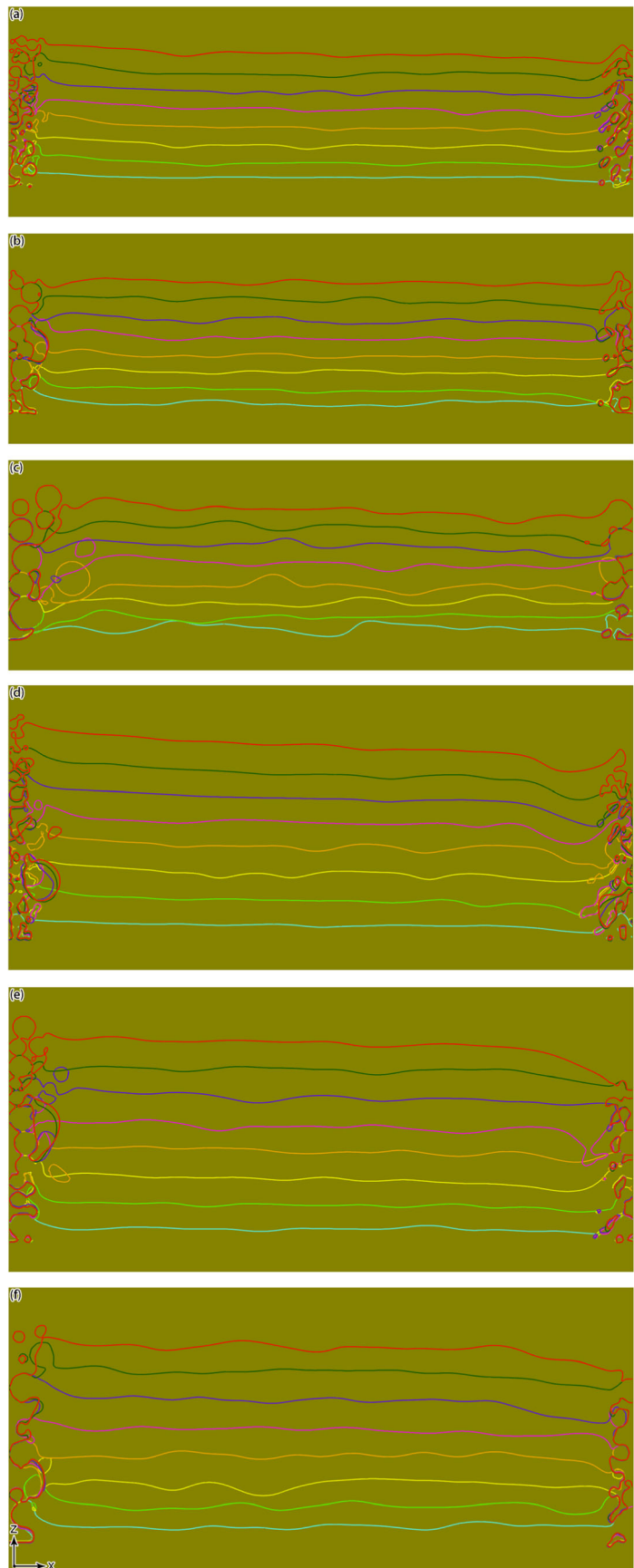
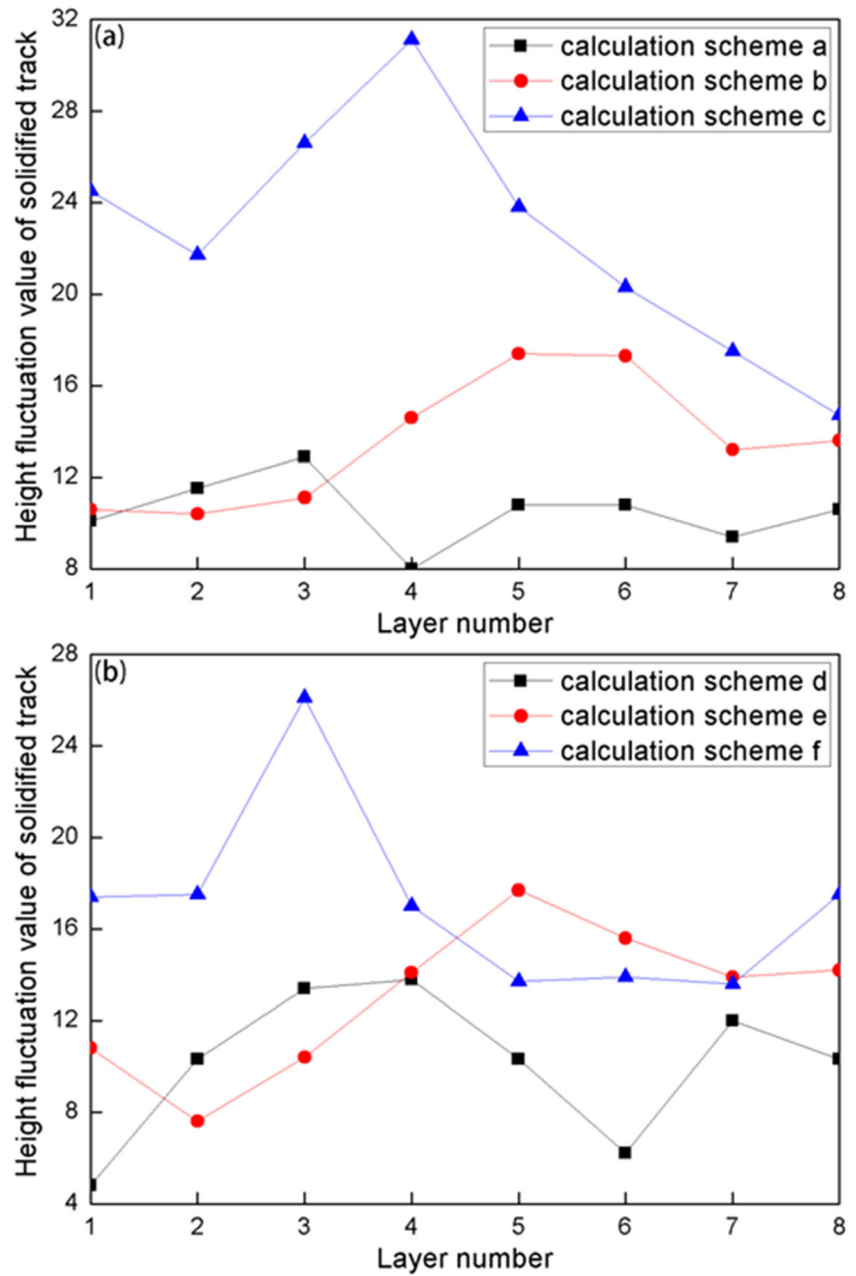


Fig. 8 Height fluctuation value of each layer of solidified track under each calculation scheme (unit: μm): **a** spreading layer thickness is $30\ \mu\text{m}$ (calculation schemes a, b, and c); **b** spreading layer thickness is $45\ \mu\text{m}$ (calculation schemes d, e, and f)

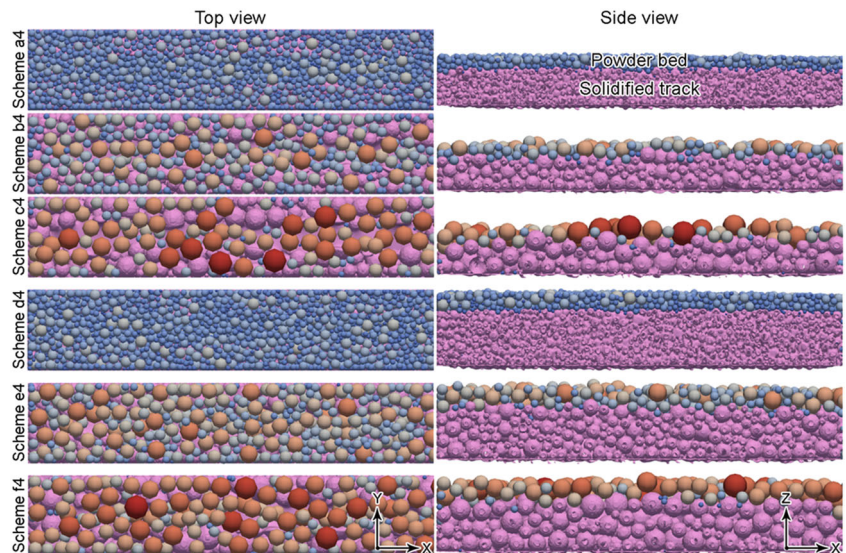


thickness has little effect on the surface roughness of the formed layer.

In order to quantitatively analyze the above results, it is believed that the solidified track height fluctuation value (the difference between the maximum and minimum Z-axis heights) in the middle section can be used to reflect the degree of solidified track height fluctuation, and Fig. 8 shows the height fluctuation value of each layer of solidified track under each calculation scheme. It can be clearly seen from the comparison results that when the spreading layer thickness was constant, the solidified track height fluctuation value was the smallest when the particle size distribution was type A, and the maximum when the particle size distribution was type C.

The reason is that compared with the particle size distribution types B and C, when the particle size distribution was type A, the average particle size was smaller, and the proportion of small-size particles was obviously higher. Because the small-size particles were easy to fill the voids during the spreading powder process, and it was not easy to form obvious protrusions, so the powder bed obtained when the particle size distribution was type A had high tightness and smooth surface (Fig. 9), and then a solidified track with a small surface height fluctuation value was obtained. Table 3 shows the average values of solidified track height fluctuations for each calculation scheme. It can be seen that when the spreading layer thickness was constant, as the proportion of large-size

Fig. 9 Particles distribution required to form the fourth layer of powder bed under each calculation scheme (red particles are large-size particles, and blue particles are small-size particles)



particles increased, the solidified track height fluctuations increased, and when the particle size distribution was constant, the fluctuation degree of the solidified track height under different spreading layer thicknesses was basically the same. In summary, when the proportion of large-size particles increases, the surface roughness of the formed layer will increase; when the particle size distribution was constant, the surface roughness of different formed layers is basically the same, and it is less affected by the spreading layer thickness.

3.3 Influence of particle size distribution on actual thickness of powder layer and depth of solidified track

Due to the gaps between the particles, the height of the solidified track obtained after the laser action must be lower than the height of the powder bed, therefore, when the roller rises to a certain spreading layer thickness and then spreads the powder bed, the actual thickness of the powder layer obtained must be greater than the set spreading layer thickness. In order to analyze the influences of particle size distribution and spreading layer thickness on the actual thickness of the powder layer and the depth of the solidified track, MATLAB

software was used to extract the average height of the top surface of each formed layer under each calculation scheme in Fig. 7, as shown in Fig. 10. On the basis of Fig. 10, subtracting the bottom surface height of the roller from the top surface height of the previous solidified track, the actual average thickness of each powder layer under each calculation scheme could be obtained, as shown in Fig. 11. On the basis of Fig. 10, subtracting the top surface height of the current solidified track from the top surface height of the previous solidified track, the depth of each layer of solidified track under each calculation scheme could be obtained, as shown in Fig. 12. It can be seen from Fig. 10 that for a particular calculation scheme, as the number of the forming layer increased, the top surface height of solidified tracks basically maintained a linear increase. In addition, the top surface height of the solidified track was mainly affected by the spreading layer thickness. The reason is obvious, that is, the greater the spreading layer thickness, the more metal particles the laser would act on, which made the top surface of the solidified track higher. When the spreading layer thickness was constant, there were only slight differences in the top surface height of the solidified track under different particle size distributions. It can be seen from the partial enlarged view in Fig. 10 that the top

Table 3 Average values of solidified track height fluctuations for each calculation scheme

Particle size distribution	Spreading layer thickness (μm)	Average value of solidified track height fluctuation (μm)
Type A	30	10.5
Type B	30	13.5
Type C	30	22.5
Type A	45	10.1
Type B	45	13.1
Type C	45	22.7

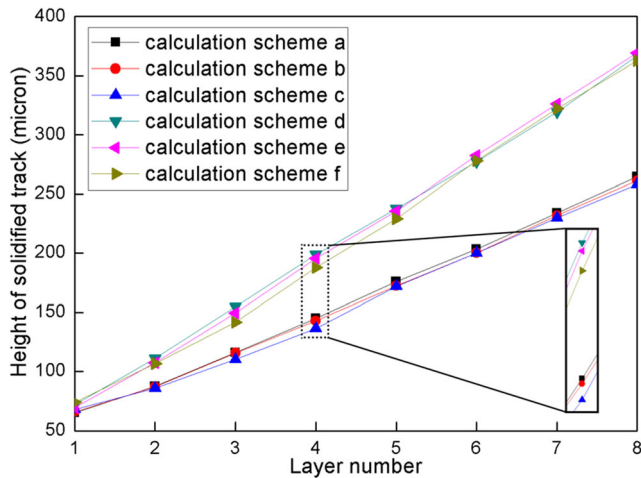


Fig. 10 Average height of the top surface of each formed layer under each calculation scheme (the height coordinate of the bottom surface of the substrate is 0 μm)

surface of the solidified track was the highest when the particle size distribution was type A. The reason is that the small-size particles in type A accounted for a larger proportion, which made the powder bed more compact.

It can be seen from Fig. 11 that for a specific calculation scheme, as the number of the forming layer gradually increased, the actual thickness of the powder bed also increased. When the fifth forming layer was reached, the actual thickness of the powder bed remained basically stable. In addition, the actual thickness of the powder bed was greatly affected by the spreading layer thickness, but less affected by the particle size distribution. It can be seen from Fig. 12 that the changing law of the depth of the solidified track is consistent with the actual thickness of the powder bed. In order to further explain this law, it can be ideally considered that the actual thickness of the powder layer T_{powder} and the depth of the solidified track D_{track} are

completely determined by the spreading layer thickness ϕ and the tightness of the powder bed ω , which can be obtained:

$$T_{powder}^N = \phi + T_{powder}^{N-1}(1-\omega) \tag{12}$$

$$D_{track}^N = T_{powder}^N \omega \tag{13}$$

where, T_{powder}^N and D_{track}^N are the actual thickness of the powder layer and the depth of the solidified track of the Nth layer, respectively. Figure 13 shows the actual thickness of each powder layer and the depth of each solidified track under different spreading layer thicknesses (30 μm and 45 μm) calculated by Eqs. 12 and 13 when the powder bed tightness was 0.6. Comparing Fig. 11 with Fig. 13a and Fig. 12 with Fig. 13b, it is not difficult to find that the change law was basically the same. From Eqs. 12 and 13, it can be easily calculated that the actual thickness of the powder layer and the depth of the solidified track will approach ϕ/ω and ϕ , respectively. When the powder bed tightness is 0.6 and the spreading layer thickness is 30 μm, the actual thickness of the powder layer and the depth of the solidified track will approach 50 μm and 30 μm, respectively, and when the powder bed tightness is 0.6 and the spreading layer thickness is 45 μm, the actual thickness of the powder layer and the depth of the solidified track will approach 75 μm and 45 μm, respectively. From the view of the numerical value, the stable values in Figs.11 and 12 are basically in line with theoretical calculations. In summary, the actual thickness of the powder layer and the depth of the solidified track are mainly related to the spreading layer thickness, but are less affected by the particle size distribution. When the fifth forming layer is reached, the actual thickness of the powder bed and the depth of the solidified track remain basically stable, which theoretically approach the ratio of the spreading layer thickness to the tightness of the powder bed and the spreading layer thickness, respectively.

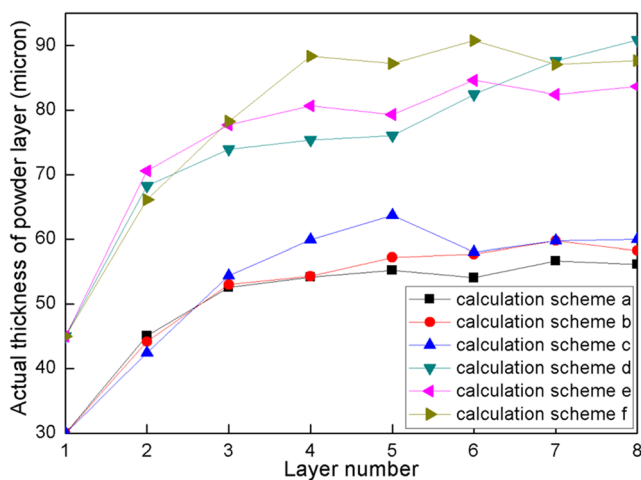


Fig. 11 Actual thickness of each powder layer under each calculation scheme

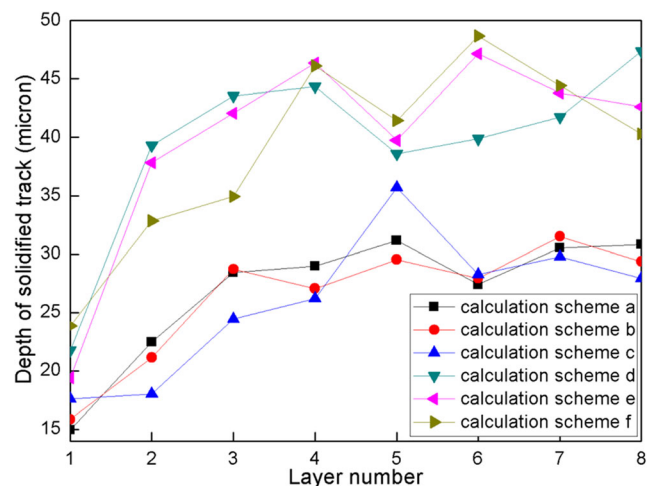


Fig. 12 Depth of each solidified track under each calculation scheme

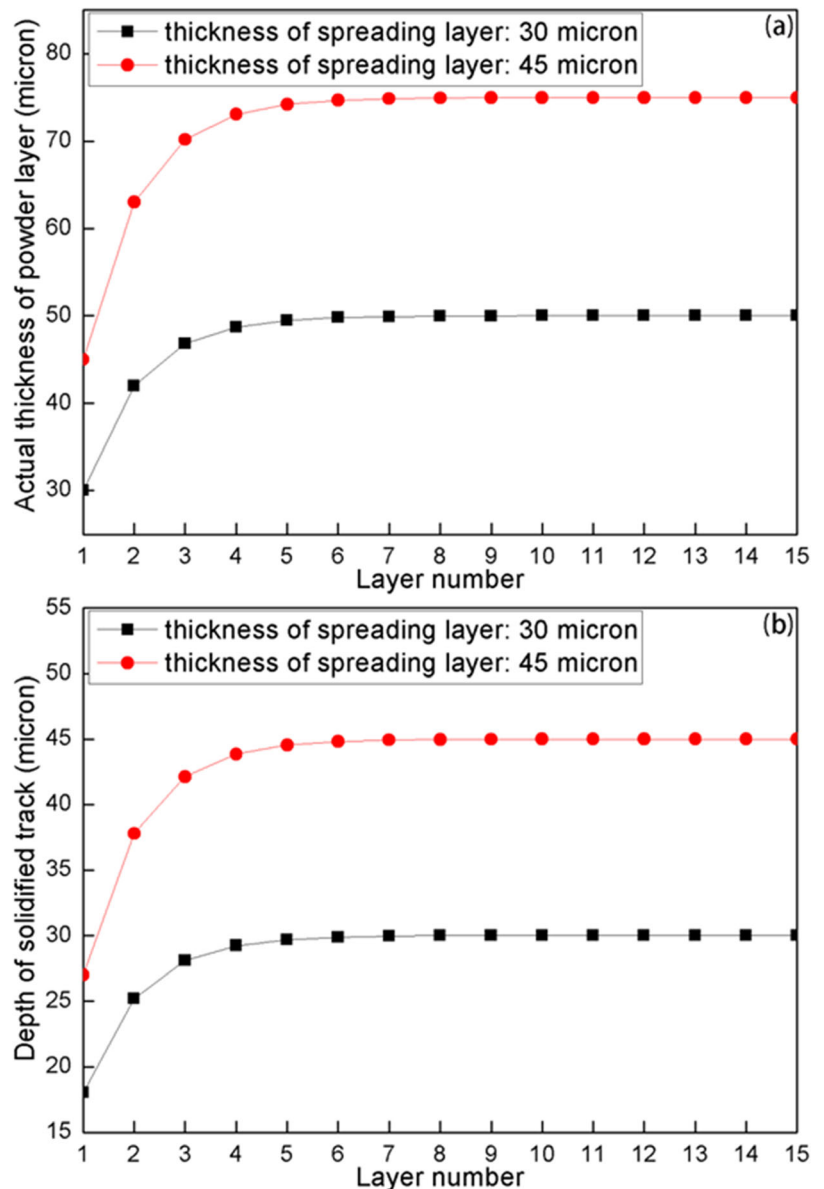
3.4 Influence of particle size distribution on porosity of formed zone

Section 3.2 has drawn the relevant conclusions that the particle size distribution affects the surface roughness of the formed layer. In order to further explore the influence of particle size distribution on the porosity of the formed zone, the forming process of calculation scheme c5 was analyzed first. Figure 14 shows the metal-phase distributions at different times under calculation scheme c5. When $t = 0\mu s$, due to the large fluctuation of the top surface of the previous solidified track, large gaps were likely to exist in the current powder bed (pink circle area); when $t = 340\mu s$, the laser acted on the large gap, but the gas was difficult to completely exhaust; when $t = 410\mu s$, the gas that could not be exhausted was drawn into the molten pool; when $t = 1000\mu s$, the gas in the molten pool

could not escape smoothly and eventually formed pore defects. So, it can be concluded that the particle size distribution has an important influence on pore defects.

Figure 15 shows the final distribution of pore defects under each calculation scheme. Here, the distribution of pore defects on the Y-direction middle section was used to approximate the porosity of the formed zone. It can be seen from the comparison results that when the spreading layer thickness was $30\mu m$, the pore defect when the particle size distribution was type A was the least, and when the particle size distribution was type B, the pore defect was the most. When the spreading layer thickness was $45\mu m$, the pore defect when the particle size distribution was type A was the least, and when the particle size distribution was type C, the pore defect was the most. The reason is that when the spreading layer thickness was small, because the actual thickness of the powder layer was

Fig. 13 Actual thickness of each powder layer and depth of each solidified track under different spreading layer thicknesses calculated by theory



small, the metal particles under the laser action were all heated and melted. At this time, the main reason for the formation of pore defect was that the gas was difficult to effectively escape the molten pool. So when the proportion of small-size particles was higher, the inter-particle voids could be effectively filled, making the powder bed more compact, and ultimately obtaining fewer pore defects, and it should be pointed out that the proportion of small-size particles with particle size distribution type A is the highest, and the proportion of small-size particles with type B is the lowest. When the spreading layer thickness was large, the actual thickness of the powder layer was large, and the main reason for the formation of pore defect at this time was that the large-size particles could not be

completely heated and melted, resulting in insufficient fusion between the formed layers, and finally forming pore defect. And it should be pointed out that the proportion of large-size particles with particle size distribution type A was the lowest, and the proportion of large-size particles with type C was the highest. Table 4 shows the volume ratio of pores (obtained by the simulation) and relative density (obtained by the experiment [9]) of parts under each calculation scheme, and the experiment results can draw conclusions consistent with the simulation results. In summary, when the spreading layer thickness is small, the pore defects are mainly affected by the proportion of small-size particles, that is, the higher the proportion of small-size particles, the lower the porosity of the

Fig. 14 Pore defect caused by excessive surface roughness under calculation scheme c5 (in the figure, red represents the metal-phase, blue represents the gas-phase; the yellow curve is the boundary of the molten pool; the pink circle is used to highlight the pore evolution process)

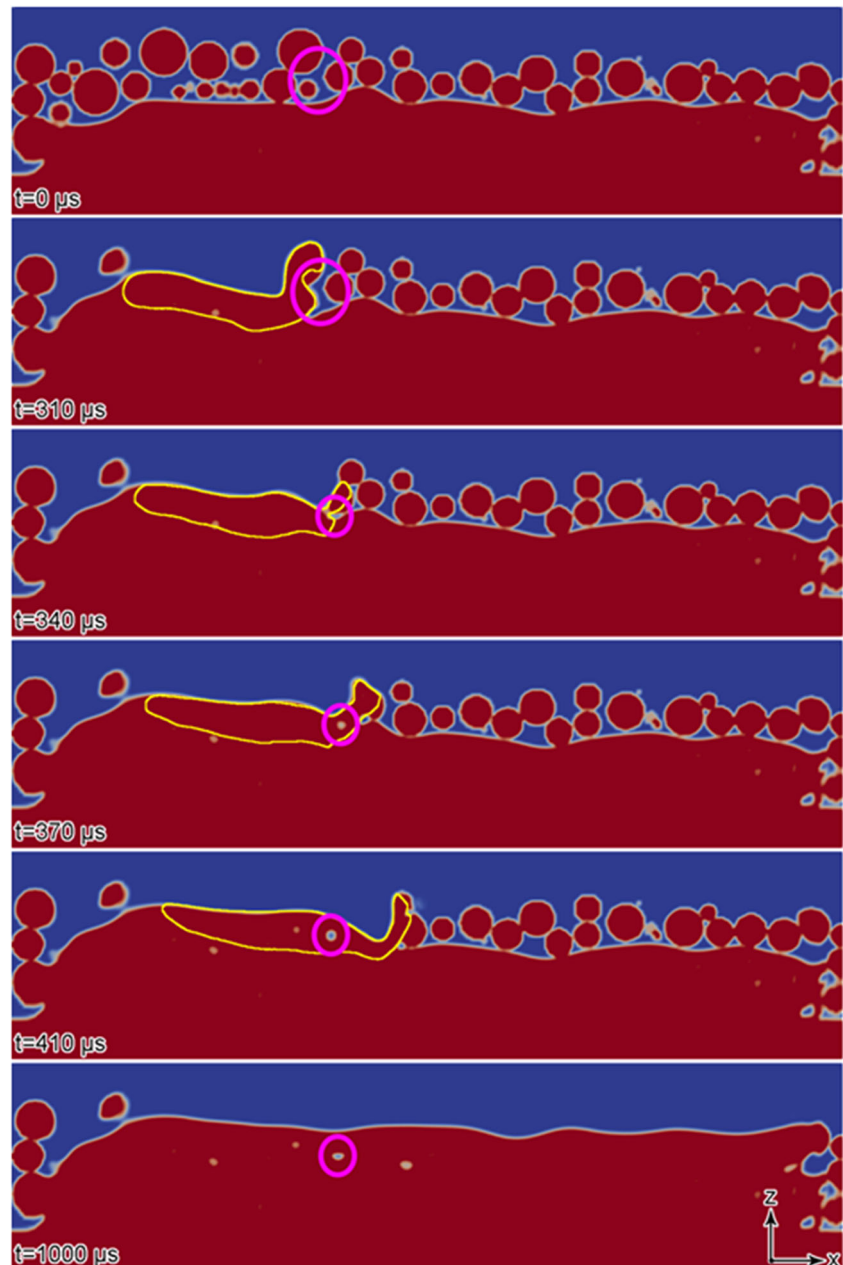
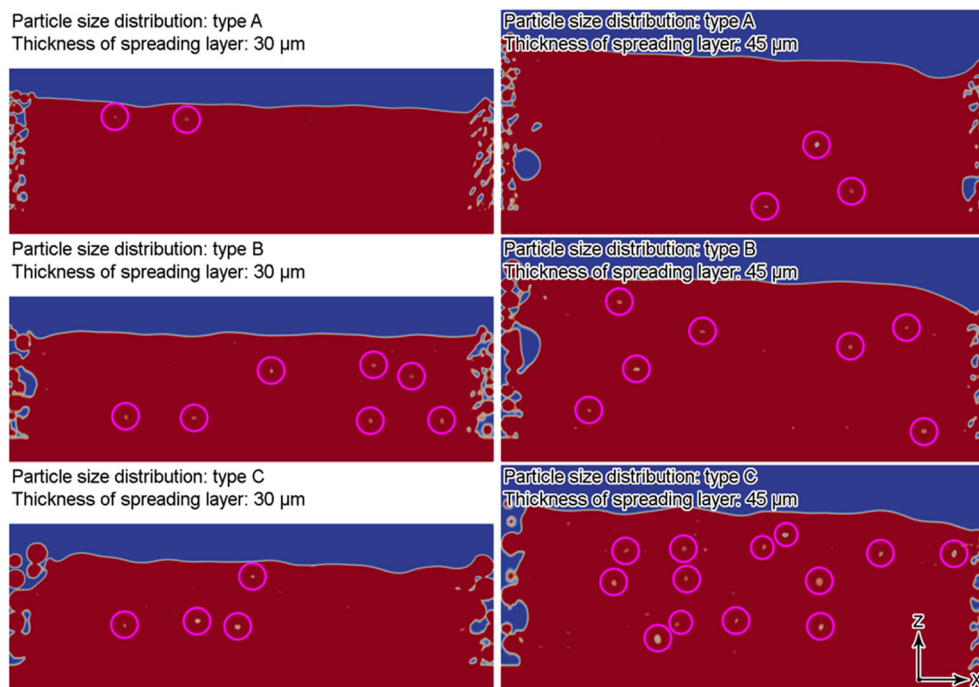


Fig. 15 Distribution of pore defects on the *Y*-direction middle section of the formed zone under each calculation scheme (the pink circles are used to mark out the pores)



formed zone; when the spreading layer thickness is large, the pore defects are mainly affected by the proportion of large-size particles, that is, the lower the proportion of large-size particles, the lower the porosity of the formed zone.

4 Conclusions

(1) Based on the open-source DEM framework Yade and the open-source FVM framework OpenFOAM, the simulation flow of the LPBF multi-layer single-track process was established, and the meso-scale forming process of the first eight layers of powder bed calculated. Among them, the considered force influence factors included gasification recoil, surface tension, Marangoni effect, viscous force, mushy zone drag force, and gravity, and the considered thermal influence factors included gasification, convection, and radiation heat dissipation.

- (2) Regarding the surface roughness of the formed layer, when the proportion of large-size particles increases, the surface roughness of the formed layer will increase; when the particle size distribution was constant, the surface roughness of different formed layers is basically the same, and it is less affected by the spreading layer thickness.
- (3) Regarding the actual thickness of the powder layer and the depth of the solidified track, they are mainly related to the spreading layer thickness, but are less affected by the particle size distribution. When the fifth forming layer is reached, the actual thickness of the powder bed and the depth of the solidified track remain basically stable, which theoretically approach the ratio of the spreading layer thickness to the tightness of the powder bed and the spreading layer thickness, respectively.
- (4) Regarding the porosity of the formed zone, when the spreading layer thickness is small, the higher the

Table 4 Volume ratio of pores (obtained by the simulation) and relative density (obtained by the experiment [9]) of parts under each calculation scheme

Particle size distribution	Spreading layer thickness (μm)	Volume ratio of pores	Relative density of part [9]
Type A	30	0.6%	99.5%
Type B	30	5.1%	95.1%
Type C	30	1.6%	98.5%
Type A	45	1.2%	98.7%
Type B	45	2.4%	97.8%
Type C	45	3.5%	96.8%

proportion of small-size particles, the lower the porosity of the formed zone; when the spreading layer thickness is large, the lower the proportion of large-size particles, the lower the porosity of the formed zone.

Author contribution Liu Cao (conceptualization, methodology, formal analysis, investigation, writing—original draft preparation, writing—review and editing, supervision), Wei Guan (conceptualization).

Funding This work was supported by the Natural Science Foundation of Guangdong Province (no. 2019A1515012040).

Data availability The data may be available upon reasonable request.

Code availability The data may be available upon reasonable request.

Declarations

Ethics approval Not applicable.

Consent to participate Not applicable.

Consent to publish Not applicable.

Competing interests The authors declare no competing interests.

References

- Cao L (2017) Numerical simulation of liquid-solid conversion affecting flow behavior during casting filling process. *Acta Metall Sin* 53:1521–1531
- Khorasani A, Gibson I, Veetil JK, Ghasemi AH (2020) A review of technological improvements in laser-based powder bed fusion of metal printers. *Int J Adv Manuf Tech* 108:191–209. <https://doi.org/10.1007/s00170-020-05361-3>
- Poorganji B, Ott E, Kelkar R, Wessman A, Jamshidinia M (2020) Review: materials ecosystem for additive manufacturing powder bed fusion processes. *JOM* 72:561–576
- Fotovvati B, Namdari N, Dehghanghadikolaei A (2019) Fatigue performance of selective laser melted Ti6Al4V components: state of the art. *Mater Res Express* 6:012002
- Slotwinski JA, Garboczi EJ, Stutzman PE, Ferraris CF, Watson SS, Peltz MA (2014) Characterization of Metal Powders Used for Additive Manufacturing. *J Res Natl Inst Stan* 119:460–493
- Pragana JP, Pombinha P, Duarte VR, Rodrigues TA, Oliveira JP, Braganca IM, Santos TG, Miranda RM, Coutinho L, Silva CM (2020) Influence of processing parameters on the density of 316L stainless steel parts manufactured through laser powder bed fusion. *Proceedings of the Institution of Mechanical Engineers Part B: Journal of Engineering Manufacture* 234:1246–1257. <https://doi.org/10.1177/0954405420911768>
- Zhang L, Zhu HH, Zhang SS, Wang GQ, Zeng XY (2019) Fabricating high dimensional accuracy LPBFed Ti6Al4V part by using bi-parameter method. *Opt Laser Technol* 117:79–86
- Maamoun AH, Xue YF, Elbestawi MA, Veldhuis SC (2018) Effect of selective laser melting process parameters on the quality of Al alloy parts: powder characterization, density, surface roughness, and dimensional accuracy. *Materials* 11:2343
- Spierings AB, Levy G (2009) Comparison of density of stainless steel 316L parts produced with selective laser melting using different powder grades. *Proceedings of SFF Symposium, Austin*
- Qiu CL, Panwisawas C, Ward M, Basoalto HC, Brooks JW, Attallah MM (2015) On the role of melt flow into the surface structure and porosity development during selective laser melting. *Acta Mater* 96:72–79
- Liverani E, Toschi S, Ceschini L, Fortunato A (2017) Effect of selective laser melting (SLM) process parameters on microstructure and mechanical properties of 316L austenitic stainless steel. *J Mater Process Tech* 249:255–263
- Makoana NW, Yadroitsava I, Möller H, Yadroitsev I (2018) Characterization of 17-4PH single tracks produced at different parametric conditions towards increased productivity of LPBF Systems—the effect of laser power and spot size upscaling. *Metals* 8:475
- Panwisawas C, Qiu CL, Sovani Y, Brooks JW, Attallah MM, Basoalto HC (2015) On the role of thermal fluid dynamics into the evolution of porosity during selective laser melting. *Scripta Mater* 105:14–17
- Zhou X, Wang DZ, Liu XH, Zhang DD, Qu SL, Ma J, London G, Shen ZJ, Liu W (2015) 3D-imaging of selective laser melting defects in a Co-Cr-Mo alloy by synchrotron radiation micro-CT. *Acta Mater* 98:1–16
- Zhang HM, Gu DD, Ma CL, Guo M, Wang R, Yang JK, Ge Q (2020) Microstructure and tribological property of selective laser melted Ni-based composites using different scanning strategies. *Vacuum* 177:109439
- Sutton AT, Kriewall CS, Leu MC, Newkirk JW (2016) Powder characterisation techniques and effects of powder characteristics on part properties in powder-bed fusion processes. *Virtual Phys Prototy* 12:3–29
- Arisoy YM, Criaes LE, Özel T, Lane B, Moylan S, Donmez A (2017) Influence of scan strategy and process parameters on microstructure and its optimization in additively manufactured nickel alloy 625 via laser powder bed fusion. *Int J Adv Manuf Tech* 90:1393–1417
- Pang SY, Chen X, Li W, Shao XY, Gong SL (2016) Efficient multiple time scale method for modeling compressible vapor plume dynamics inside transient keyhole during fiber laser welding. *Opt Laser Technol* 77:203–214
- Yin J, Wang DZ, Yang LL, Wei HL, Dong P, Ke LD, Wang GQ, Zhu HH, Zeng XY (2020) Correlation between forming quality and spatter dynamics in laser powder bed fusion. *Addit Manuf* 31:100958
- Gunenthiram V, Peyre P, Schneider M, Dal M, Coste F, Koutiri I, Fabbro R (2018) Experimental analysis of spatter generation and melt-pool behavior during the powder bed laser beam melting process. *J Mater Process Tech* 251:376–386
- Escano LI, Parab ND, Xiong LH, Guo QL, Zhao C, Sun T, Chen LY (2019) Investigating Powder Spreading Dynamics in Additive Manufacturing Processes by In-situ Highspeed X-ray Imaging. *Synchrotron Radiat News* 32:9–13
- Hojjatzadeh SMH, Parab ND, Yan WT, Guo QL, Xiong LH, Zhao C, Qu ML, Escano LI, Xiao XH, Fezzaa K, Everhart W, Sun T, Chen LY (2019) Pore elimination mechanisms during 3D printing of metals. *Nat Commun* 10:3088
- Kyogoku H, Ikeshoji T-T (2020) A review of metal additive manufacturing technologies: Mechanism of defects formation and simulation of melting and solidification phenomena in laser powder bed fusion process. *Mech Engineering Rev* 7:19–00182
- Zhang Y, Zhang J (2019) Modeling of solidification microstructure evolution in laser powder bed fusion fabricated 316L stainless steel using combined computational fluid dynamics and cellular automata. *Addit Manuf* 28:750–765

25. Khairallah SA, Anderson AT, Rubenchik A, King WE (2016) Laser powder-bed fusion additive manufacturing: physics of complex melt flow and formation mechanisms of pores, spatter, and denudation zones. *Acta Mater* 108:36–45
26. Gu DD, Xia MJ, Dai DH (2019) On the role of powder flow behavior in fluid thermodynamics and laser processability of Ni-based composites by selective laser melting. *Int J Mach Tool Manu* 137: 67–78
27. Parteli EJR, Pöschel T (2016) Particle-based simulation of powder application in additive manufacturing. *Powder Technol* 288:96–102
28. Liu BQ, Fang G, Lei LP, Liu W (2020) A new ray tracing heat source model for mesoscale CFD simulation of selective laser melting (SLM). *Appl Math Model* 79:506–520
29. Cao L (2020) Mesoscopic-scale simulation of pore evolution during laser powder bed fusion process. *Comp Mater Sci* 179:109686
30. Cao L (2019) Numerical simulation of the impact of laying powder on selective laser melting single-pass formation. *Int J Heat Mass Tran* 141:1036–1048
31. Wang ZK, Yan WT, Liu WK, Liu MB (2019) Powder-scale multi-physics modeling of multi-layer multi-track selective laser melting with sharp interface capturing method. *Comput Mech* 63:649–661
32. Zheng M, Wei L, Chen J, Zhang Q, Zhong CL, Lin X, Huang WD (2019) A novel method for the molten pool and porosity formation modelling in selective laser melting. *Int J Heat Mass Tran* 140: 1091–1105
33. Tang C, Tan JL, Wong CH (2018) A numerical investigation on the physical mechanisms of single track defects in selective laser melting. *Int J Heat Mass Tran* 126:957–968
34. Zheng M, Wei L, Chen J, Zhang Q, Li JQ, Sui S, Wang G, Huang WD (2019) Surface morphology evolution during pulsed selective laser melting: Numerical and experimental investigations. *Appl Surf Sci* 496:143649
35. Panwisawas C, Qiu CL, Anderson MJ, Sovani Y, Turner RP, Attallah MM, Brooks JW, Basoalto HC (2017) Mesoscale modelling of selective laser melting: Thermal fluid dynamics and microstructural evolution. *Comp Mater Sci* 126:479–490
36. Cao L (2020) Numerical simulation including the influence of process parameters on SLM single-layer multi-pass formation. *Metall Mater Trans A* 51:4130–4145
37. Cao L (2019) Study on the numerical simulation of laying powder for selective laser melting process. *Int J Adv Manuf Tech* 105: 2253–2269
38. Le KQ, Tang C, Wong CH (2019) On the study of keyhole-mode melting in selective laser melting process. *Int J Therm Sci* 145: 105992
39. Cao L, Liao DM, Sun F, Chen T, Teng ZH, Tang YL (2017) Prediction of gas entrapment defects during zinc alloy high-pressure die casting based on gas-liquid multiphase flow model. *Int J Adv Manuf Tech* 94:807–815
40. Cao L (2021) Numerical investigation on molten pool dynamics during multi-laser array powder bed fusion process. *Metall Mater Trans A* 52:211–227

Publisher's note Springer Nature remains neutral with regard to jurisdictional claims in published maps and institutional affiliations.